Check for updates

Shinjan Ghosh[1]
Mem. ASME
Department of Mechanical and
Aerospace Engineering,
University of Central Florida,
Orlando, FL 32816
e-mail: shinjanju.ucf.edu@knights.ucf.edu

Ryan Wardell
Mem. ASME
Department of Mechanical and
Aerospace Engineering,
University of Central Florida,
Orlando, FL 32816
e-mail: wardrummer97@knights.ucf.edu

Sudeepta Mondal
Mem. ASME
Department of Mechanical Engineering and
Department of Mathematics,
The Pennsylvania State University,
329 Reber Building,
University Park, PA 16802
e-mail: sudeepta979@gmail.com

Erik Fernandez
Department of Mechanical and
Aerospace Engineering,
University of Central Florida,
Orlando, FL 32816
e-mail: erik.fernandez@ucf.edu

Asok Ray
Fellow ASME
The Pennsylvania State University,
329 Reber Building,
University Park, PA 16802
e-mail: axr2@psu.edu

Jayanta Kapat
Mem. ASME
Department of Mechanical and
Aerospace Engineering,
University of Central Florida,
Orlando, FL 32816
e-mail: jayanta.kapat@ucf.edu

Topology Optimization and Experimental Validation of an Additively Manufactured U-Bend Channel

Serpentine channels are a common feature seen in heat ex-changer geometries. For example, they are present in midchord regions of gas turbine blades to prevent material failure at high turbine inlet temperatures. Due to their serpentine nature, these channels contain 180 deg turns or U-bends. These U-bends are responsible for nearly 20% of the pressure drop in such channels (Verstraete et al., 2013, "Optimization of a U-Bend for Minimal Pressure Loss in Internal Cooling Channels-Part I: Numerical Method," ASME J. Turbomach., ***135****(5), p. 051015). A topology optimization (TO) method has been used in this study to optimize the shape of a baseline U-bend for minimum pressure drop, at a Reynolds number of 17,000. TO uses a variable permeability approach to design an optimum flow-path by manipulation of solid blockage distribution in the flow-path. The pressure drop across the channel was lowered by 50% when compared to a standard U-bend channel profile from literature. Postprocessing was performed to extract the flow-path and run a forward simulation in* STAR-CCM+ *after remeshing with wall refinement. A 3D printed model of the TO shape and benchmark U-bend was created using acrylonitrile butadiene styrene as the printing material, to confirm the results of the turbulent fluid TO, which is a relatively untouched topic in current TO literature. Experimental results showed deviation from computational fluid dynamics (CFD) by about 5%. Comparison of the TO optimum was carried out with an in-house parametric shape optimization using surrogate model-based Bayesian optimization (BO) and a similar shape optimization study from literature. A higher reduction in pressure drop was seen in the case of the TO geometry when compared to the benchmark and the BO cases.*
[DOI: 10.1115/1.4052928]

Introduction

Internally cooled modern gas turbine blades need high-efficiency cooling performance due to the requirement of high turbine inlet temperatures. At an optimum pressure ratio, high turbine inlet temperature helps increase the thermodynamic efficiency of gas turbine cycles, but the gain in efficiency can be undone by the high pumping power required by the compressor to flow cooling air through these channels [1]. U-bends are crucial to the performance of these channels since these turns cause the formation of counter-rotating Dean vortices [2] which increases turbulent mixing, resulting in high heat transfer but also high-pressure drop. Metgzger [3] performed one of the earlier experimental studies on a U-bend using pressure tap measurements and flow visualization. Parameters like turn clearance, turning radius, and channel aspect ratios were found to affect the pressure drop. Formation of separation bubbles was detected in these channels, the size of which was a direct contributor to the magnitude of pressure loss. The formation of symmetric counter-rotating Dean vortices near 180 turns was recorded by Son et al. [4] using particle image velocimetry in a two-pass channel. The strength of the vortices was found to increase from the beginning to the end of the turn. Laser Doppler velocimetry studies by Liou et al. [5] showed an acceleration of flow near the inner wall and deceleration at the outer wall of the channel. This confirms the presence of a radial pressure gradient at the turn, which also causes the formation of the symmetric counter-rotating Dean vortexes due to the flow rolling up. Change in divider wall thickness was found to cause shifts in the peak of near-wall turbulent kinetic energy (TKE), explaining the effect wall thickness has on pressure drop performance. The introduction of turning vanes to bent flow

[1]Corresponding author.

Contributed by the Fluids Engineering Division of ASME for publication in the Journal of Fluids Engineering. Manuscript received July 9, 2021; final manuscript received October 30, 2021; published online February 17, 2022. Assoc. Editor: Stefan aus der Wiesche.

 Copyright © 2022 by ASME

Downloaded from http://asmedigitalcollection.asme.org/fluidsengineering/article-pdf/144/7/071206/6849053/fe_144_07_071206.pdf by The Pennsylvania State University user on 21 October 2022

ducts has shown lower pressure drop in existing literature [6–8]. Chu et al. [6] showed a reduction of pressure drop with a significant change in separation and re-attachment patterns for stationary and rotating U-bend channels. Schuler et al. [7] showed that a given combination of multiple turning vanes can cause a 25% reduction in pressure loss, however wrong positioning of the vanes can also result in an increase of the same. Incompressible Reynolds-averaged Navier–Stokes (RANS) studies on 90 deg pipe bends by Valsala et al. [8] showed that the introduction of vanes in channel bends reduces pressure drop by stabilizing flow and reducing turbulence. It is important to account for numerical studies performed on U-bend channels since this study uses a computational fluid dynamics (CFD) based approach for design optimization. Various turbulence modeling techniques used in the past include RANS simulations with Eddy-viscosity models (k–ϵ and k–ω) or Reynolds stress models and high fidelity large eddy simulations (LES) simulations. Sleiti et al. [9] concluded that Reynolds stress models (RSM) models showed better performance compared to RANS models, as anisotropy is taken into account while modeling turbulent fluctuations. LES simulations were found to have good agreement with experimental laser Doppler velocimetry data by Sewall et al. [10] from 180 deg bend regions. However, the high computation cost of LES simulations deems it unsuitable for use in this study. Although eddy-viscosity models are often found to wrongly predict local turbulent flow phenomenon [11], a comparative study between two-equation eddy viscosity models and RSM models showed that the overall pressure drop prediction performance of these models are suitable for optimization problems. Given the quicker computation time and easier convergence of the k–ϵ models, they are a clear favorite for design optimization studies.

Nearly 20% of the pressure drop in serpentine passage cooling channels occurs due to the U-bends [12]. For this reason, optimizing the geometry of these U-bends is key to efficient internal cooling. Surrogate models based optimization was performed by Verstraete et al. [12] to minimize pressure drop by changing inner and outer wall shapes, which were parameterized using Bezier curves. The end result was a 37% reduction of pressure drop. Experimental validation was performed on this optimized shape and baseline, in a subsequent study [13], using particle image velocimetry techniques. Topology optimization was carried out by Ghosh et al. [14] with the goal of minimizing pressure drop and maximizing heat transfer. The fluid path was altered and curved walls were created at the bends to minimize separation zones. Similar results were shown by Dilgen et al. [15], where a 2D U-bend optimization saw about 50% reduction in pressure drop.

Topology optimization is used in this study to create a U-bend design that has minimum pressure drop. Fluid topology optimization (TO) is a relatively newer topic of research compared to structural TO [16], which has been studied for decades. TO deals with the distribution of materials in a domain to optimize an assigned objective function. Dbouk [17] and Alexanderson et al. [18], review fluid and heat transfer TO works from the last two decades. First introduced by Borvall and Peterson [19] in 2003, fluid dynamic topology optimization operates on the principle of creating the optimum fluid path by penalizing cells in the domain to effectively simulate solid blockages/regions of low permeability. Low-speed Stokes flow scenarios were the subject of study, for designing channels with minimum power loss from wall friction. Laminar Navier–Stokes problems were first tackled by Gersborg-Hansen et al. [20], using a Brinkman model of Darcy's law for porous medium flow. Another approach to modeling a TO problem is that of separating the flow domain and the porous solid domain into Stokes flow and Darcy flow, respectively, which was used by Wiker [21] and Guest et al. [22]. It was demonstrated by Bruns [23] that a volumetric penalty approach can be adapted for structural, fluid, and heat transfer TO cases. This density-dependent penalization can be used in Navier–Stokes (N-S) equations as well as thermal conductivity problems. Level set methods have been used by a number of authors [24–26] to manipulate material distributions using the zero level boundaries at solid-fluid interfaces. TO problems are known to have higher degrees-of-freedom compared to traditional parametric optimization methods since each element in the given computation domain can have its own unique value for permeability. For this reason, Lagrangian-based adjoint methods coupled with the steepest gradient search algorithms are suitable for such applications. Due to the high degree-of-freedom of the TO problem, gradient-based search algorithms are commonly used, with rare exceptions such as Yoshimura et al. [27] who used a Kriging-based gradient free method. All the above TO studies deal with low-Reynolds number or laminar flow scenarios. Turbulent flow phenomenon was first tackled by Othmer et al. [28], who used a RANS model with an adjoint solver for 3D, duct flows. A frozen turbulence model was used, without permeability adjustments in the two-equation k–ϵ model. A similar approach was taken by more recent studies by Ghosh et al. [14,29] and Pietropaoli et al. [30] to achieve heat transfer maximization and pressure drop minimization. A frozen k–epsilon turbulence modeling approach has been used in this study as well. Adjoint TO study by Kontoleontos et al. [31] used a permeability correction on the Spalart–Allmaras turbulence model. A k–epsilon model with permeability corrections was used by Dilgen et al. [15] for 2D and 3D problems related to pressure minimization and forced convection. Philippi and Jin [32] used a scaled turbulence model which scaled down the turbulent viscosity based on the fluid fraction value of a given cell. This treatment was based on an earlier study [33] which concluded that turbulent viscosity in porous media was directly proportional to the pore sizes.

The goal of this work is to use TO for optimizing a simple U-bend shape with the goal of pressure minimization. The unconventional shape created as a result of TO is fabricated using 3D printing, to validate the improvements in pressure drop. A spline parametric surrogate-based Bayesian optimization has also been carried out to understand the performance of TO compare to a more conventional approach. In addition to the above two, the pressure drop performance has also been compared with a U-bend profile from the literature.

The adjointshapeoptimizationFOAM solver in OPENFOAM has to perform TO on a baseline U-bend shape. The results obtained show a 50% reduction in the objective function when compared to a benchmark U-bend profile from literature. Postprocessing and surface smoothing was required to get rid of stair-like formations of the solid-fluid boundaries, created due to the mesh resolution of the baseline mesh. This postprocessed geometry was remeshed and simulated in STAR-CCM+ to correct possible leakage flows, lack of wall treatments, and refinements in the initial TO approach. The postprocessed shape was then used to create a 3D printed optimum flow channel for experimental testing. Dbouk [17] records that only 3% of all fluid dynamics TO studies actually deal with turbulent flows and that there is a lack of experimental data in this subject. The recent advances in additive manufacturing have made it possible to fabricate the unconventional optimum shapes formed as a result of TO. Dede et al. [34] used additively manufactured baseline and optimum geometries from TO to experimentally validate results. Additive manufacturing techniques have been introduced for manufacturing nonstructural components of gas turbines [1]. Ruiz et al. [35] performed X-ray particle tracking experiments to evaluate the velocity fields inside a laser additively manufactured blade leading edge. This design was also evaluated earlier by Calderon et al. [36]. The above generated TO design was then compared to results from alternative parametric design optimization methods, from both, in-house and literature studies. CFD-based optimization methods are traditionally known to use parametric designs for global sampling techniques such as genetic algorithm [37,38] or surrogate model-based methods [39]. A surrogate model-based parametric shape optimization has also been carried out to understand the difference in performance between TO and traditional approaches. This alternative optimization method is known to save computational time by

Downloaded from http://asmedigitalcollection.asme.org/fluidsengineering/article-pdf/144/7/071206/6849053/fe_144_07_071206.pdf by The Pennsylvania State University user on 21 October 2022

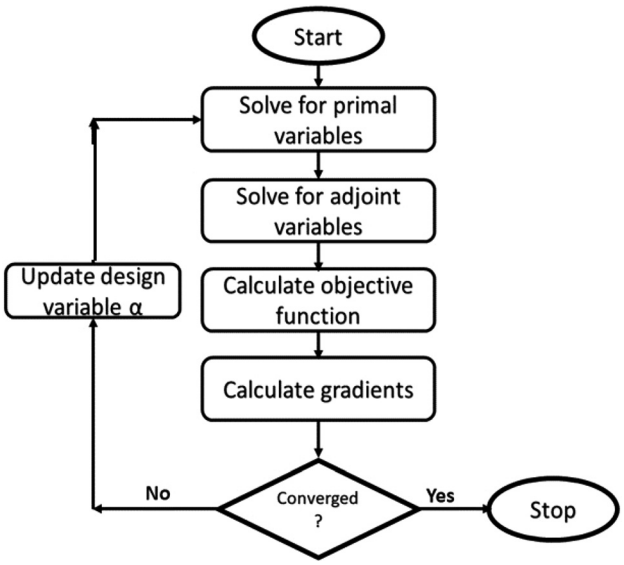

Fig. 1 Flowchart for the topology optimization process

using a surrogate model to learn the input–output relationships from initial CFD data sets sampled from the design domain. This study used a Bayesian approach to sample update points after the initially trained surrogate model, with an exploration versus exploitation strategy to arrive at an optimum. This method was previously used by Ghosh et al. [40,41] to optimize pin-fin array shapes for maximizing thermal performance and was found to be 50% faster compared to a genetic algorithm optimization study. A spline-based technique is used to parametrize the U-bend shape, similar to the method used by Verstraete et al. [12], where a kriging model and a neural network were used. Comparisons revealed higher augmentation in the objective function in addition to lower computation times in the case of TO.

Methodology

The design variable in this study is permeability, a value for which is possessed by every cell in the computational domain. The Brinkman penalization factor(α) has been used to represent permeability in each cell. Governing equations, solving for the primal fields, contain contributions from this parameter, as do the adjoint equations, which are derived from the Lagrangian multiplier expression. The steps involved in the process of topology optimization have been summarized in Fig. 1. A pre-initialized field ($\alpha = 0$) is used to start the process. The set of governing equations for the momentum, continuity, and energy are solved for the adjoint and primal variables, respectively, using this pre-initialized field. The sensitivity of the problem is calculated using a derivative of the Lagrangian multiplier expression with respect to the permeability expression. The steepest gradient algorithm is used to update the permeability fields using a user-defined step. This process is continued in a loop until convergence is observed in the final design and the objective function value.

Governing Equations. Using the Brinkman penalization factor (αu) in the Navier–Stokes equation, a permeability penalty was introduced to the problem. As seen in Fig. 2, a high value of this penalty will reduce the velocity magnitude to zero, for the respective region, due to low permeability. A zero value of α will result in the generic form of the N–S equation. The value of α (permeability factor) varies from 0, which represents the fluid domain, to a maximum value of α_{Max} representing the solid domain. For this study, an α_{Max} value of 8×10^5 was used. The momentum equations were solved using the pressure–velocity coupled semi-implicit method for pressure linked equations [42] methodology,

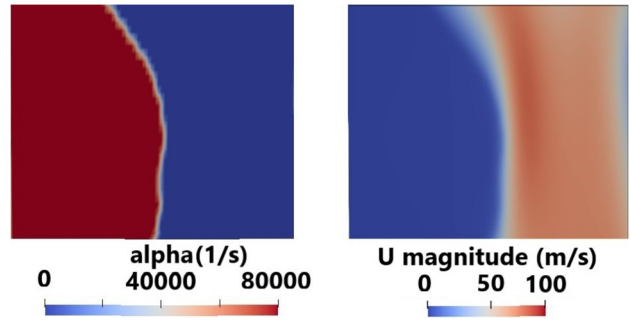

Fig. 2 Blockage simulated by material distribution. Porosity distribution (left) and velocity contour (right) of the flow field.

with temperature solved as a passive scalar at every primal flow solution, with the converged values of the pressure and velocity fields.

Navier–Stokes equation

$$R_1 = (u \cdot \nabla)u + \nabla(p)/\rho - \nabla(2\mu_{\text{eff}}D(u)) + \alpha u = 0 \tag{1}$$

where $D(u) = (\nabla\, u + (\nabla\, u)^T)\,/2$. A "frozen" K-Epsilon turbulence model has been used similar to Othmer [28]. This approach ignores the turbulent viscosity terms while calculating the sensitivity for the gradient ascent method and also doesn't include the permeability correction in the turbulence models. The standard k–ϵ model used in this study can be described as

$$\frac{D(\rho\epsilon)}{Dt} = \nabla(\rho D_\epsilon \nabla(\epsilon)) + \frac{C_1\epsilon}{k}\left(P + C_3\frac{2}{3}k\nabla U\right) - C_2\rho\frac{\epsilon^2}{k} \tag{2}$$

While the k equation

$$\frac{\partial(\rho k)}{\partial t} + \nabla(\rho u k) + \nabla^2(\rho D_k) = \rho G - \frac{2}{3}\left(\rho(\nabla.u)k\right) - \left(\rho\frac{\epsilon}{k}\right) \tag{3}$$

where D_k and D_ϵ are diffusivity rates, G is TKE production rate and $C_1 = 1.42$, $C_2 = 1.92$, $C_3 = 0$, and $C_\mu = 0.09$ are model constants.

The turbulent viscosity is calculated as

$$\nu_t = C_\mu\frac{k^2}{\epsilon} \tag{4}$$

While effective viscosity

$$\mu_{\text{eff}} = \rho(\nu + \nu_t) \tag{5}$$

Continuity equation

$$R_2 = \nabla \cdot (u) = 0 \tag{6}$$

Lagrangian Multiplier Method. The Lagrangian multiplier method has been used in the current approach to setup the optimization problem, which combines the objective function and constraints into a single equation by using adjoint variables for each constraint

$$L = F + u_a\int R_1 d\Omega + p_a\int R_2 d\Omega \tag{7}$$

where Ω is the volume domain and $d\Omega$ is a differential volume. R_1 and R_2 are the momentum and continuity equations, respectively. Such that

$$R_1 = R_2 = 0 \tag{8}$$

u_a and p_a are the adjoint variables for velocity and pressure, respectively. F is the objective function, which signifies net pressure drop across the control volume (from inlet to exit)

Downloaded from http://asmedigitalcollection.asme.org/fluidsengineering/article-pdf/144/7/071206/6849053/fe_144_07_071206.pdf by The Pennsylvania State University user on 21 October 2022

$$F = \int_{\tau} (p)(u \cdot n) d\tau \tag{9}$$

where τ represents the surface boundaries of the domain, Ω is the internal volume and n is a normal vector to each surface.

Adjoint Equations. The adjoint equations are required in the current process to calculate the adjoint multipliers which feature in the Lagrangian multiplier expression (Eq. (7)). The adjoint variables u_a and p_a can be calculated using the adjoint equations. Each adjoint equation is dependent on the primal variable, and the adjoint NS equation is a function of the adjoint pressure and velocity variables. Like the primal NS and continuity equations, the adjoints are solved using a predictor-corrector loop

$$\frac{dL}{du} = \frac{dL}{dp} = 0 \tag{10}$$

The adjoint Navier–Stokes equation is stated as

$$\rho(-\nabla(u_a) \cdot u - (u \cdot \nabla)u_a) + \nabla(p_a) - \nabla(2\mu_{eff} D(u_a)) + \alpha(u_a) + \rho c(\mathrm{Ta} \cdot \nabla T) = 0 \tag{11}$$

Similarly, the adjoint continuity equation

$$\nabla \cdot (u_a) = 0 \tag{12}$$

The Gauss divergence theorem can be used in Eq. (10) to calculate the adjoint boundary conditions, as shown in Phillipi and Jin [32]. Adjoint velocity boundary condition can be written as

$$u_a + u = 0 \tag{13}$$

For adjoint pressure

$$p_a = u \cdot u_a + u_n \cdot u_{an} + \frac{dF}{du_n} \tag{14}$$

The values of the adjoint variables are essential at every outer iteration to calculate the value of sensitivity, for the steepest descent algorithm to calculate slope. The semi-implicit method for pressure linked equations algorithm has been used to solve the incompressible Navier–Stokes equations. The geometric agglomerated algebraic multigrid solver with a Gauss upwind discretization scheme has been used to facilitate the convergence of primal and adjoint quantities, by dampening numerical oscillations.

Sensitivity Analysis. The derivative of the Lagrangian with respect to the Brinkman penalization factor α is equal to the sensitivity of the current problem. The following expression can be used to calculate the sensitivity of the current problem:

$$\text{Sensitivity} = \frac{dL}{d\alpha} = u \cdot u_a \tag{15}$$

It is seen that the sensitivity is a function of the adjoint and primal velocities. The solution for the above quantities is found using the primal and adjoint equations, respectively. The sensitivity derivative is then used in the steepest descent method to arrive at an optimum. The optimization process is stopped once the objective function reaches a constant with respect to optimization iterations and the flow geometry stops changing. The design variable update at the nth optimization step can be quantified as

$$\alpha(n) = \alpha(n-1) + \lambda \frac{dL}{d\alpha} \tag{16}$$

where user-defined step λ

$$\frac{\lambda}{\alpha_{\max}} = 1.25 \tag{17}$$

Three-Dimensional Printing and Experimental Setup

- After completion of the optimization process, the best performing/optimized U-bend shape was extracted from the CFD air-solid. A 3 mm thick shell was created in computer aided design postprocessing with 24 counterbored through holes for measuring pressure drop on the end wall along with the streamwise location, selected with knowledge of the CFD pressure fields in order to better capture the distributions in regions of high-pressure gradient. The same process was undertaken for designing a shell for the U-bend benchmark, with concurrent pressure tap locations as the optimum shape, for comparing local gradients of pressure for the two designs. These shell designs were then exported to an Standard Tessellation Language format and additively manufactured in-house, using an ULTIMAKER 2.0 EXTENDED+ fused deposition modeling printer. The whole workflow post-the TO process has been summarized in Fig. 3. In fused deposition modeling printers, a layer-by-layer extrusion approach is used to deposit heated thermoplastic filament from a nozzle. These filaments are typically heated to their melting point and the layer thickness is an operational parameter. In the current application, acrylonitrile butadiene styrene filament was used for making the baseline and optimized channels, with a layer thickness of 0.1 mm. To complete the experimental setup, a bell-mouth inlet and straight section, along with an exit section were also 3D printed. These parts were then assembled with the test section, and attached to a dump plenum box which is connected to a blower (Fig. 4). The experimental rig was run under suction, with a pitot tube 1 inch from the exit plane of the bell-mouth for test section inlet velocity measurements. The bell mouth profile was created using a fifth-order polynomial as shown in Bell and Mehta [43], with a 7.7 contraction ratio. The straight channel from the bell-mouth entry to the test section was six hydraulic diameters long. In addition to the 24 pressure measurement locations in the test section, a pressure measurement was also carried out at the U-bend exit to calculate the overall pressure drop. A

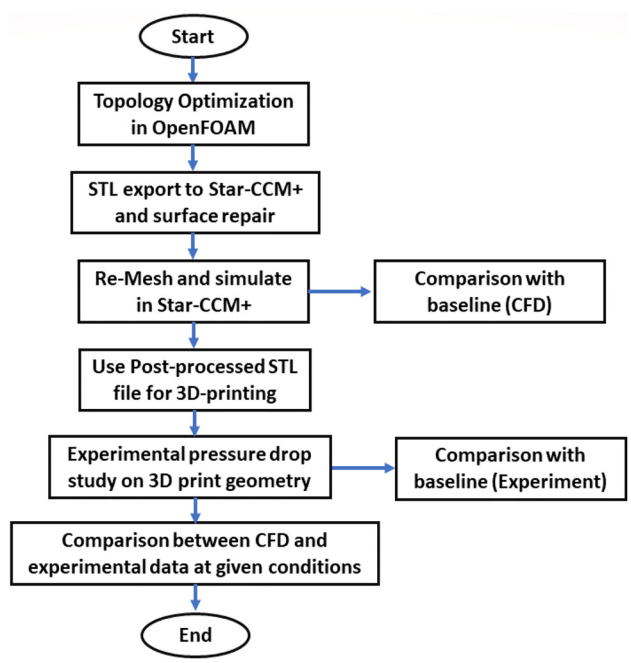

Fig. 3 Flowchart for entire work

Downloaded from http://asmedigitalcollection.asme.org/fluidsengineering/article-pdf/144/7/071206/6849053/fe_144_07_071206.pdf by The Pennsylvania State University user on 21 October 2022

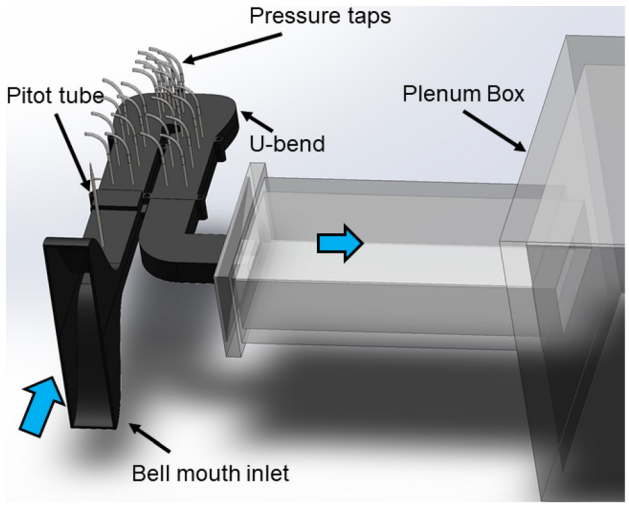

Fig. 4 Experimental setup of the suction rig for flow-testing 3D printed U-bend pieces

Fluke 922 pressure transducer was used to calculate the inlet velocity and pressure drop at each location. The Fluke 922 (Fluke corporation, Everett, WA) had a 1% error in pressure measurement for a range of 4000 Pa and a 2.5% error in velocity measurement for a range of 80 m/s. The random error in pressure drop amounted to 3.2%, thereby resulting in a 6.5% pressure drop uncertainty. A random error of 2.37% in velocity readings, along with a 1.6% bias in inlet temperature measurement (room temp 25° C) resulted in total uncertainty of 5.58% in hydraulic diameter based on Reynolds number.

Results and Discussion

Topology Optimization in OPENFOAM. The baseline U-bend shape (Fig. 5) was meshed using the blockmesh utility in OPENFOAM, for a uniformly refined domain (1×10^6 cells) to account for material distribution in previously unknown locations. The boundary conditions for this starting point had a constant inlet velocity profile of 10 m/s and a zero pressure outlet. The side and top walls of the geometry were given no-slip boundary conditions. The optimization process was subsequently carried out according to the process described in Fig. 1. A few different instances, of the evolving geometry from the optimization process, have been shown from Figs. 6–9. The flow path is extracted by choosing the regions with the lowest blockage (0–1% of α_{Max}) Low-velocity regions coincide with regions of high blockages. For Fig. 6(*a*), the formation of solid at the bottom left and right corners are visible. The morphing of the flow geometry is also seen at those locations in Fig. 6(*b*). These low permeability zones are seen to expand to larger portions in the 4000th optimization iteration (Fig. 7), with a curvature in the left-wall and rounded corners on the right. Morphing is seen for the flow-path at the inner wall as well. In the more advanced stage of iteration (Fig. 8), formations of a vane-like structure are seen to begin on the walls of the extracted flow-path. Finally, in addition to the rounded inner and outer wall corners, the optimum geometry (Fig. 9) has two vane-like solid blockages as seen in both, the midplane velocity plot and the extracted flow path. As seen in the optimization iterations versus exit pressure plot (Fig. 10), the process is halted after the formation of a plateau which is seen after the 10,000th iteration. A 53% reduction in pressure drop is obtained, when compared to the benchmark U-bend shape (Fig. 5). The formation of a turning vane with optimization iterations can be seen in Fig. 11. In the 2000th iteration (Fig. 11(*a*)), the end wall is seen to be smooth

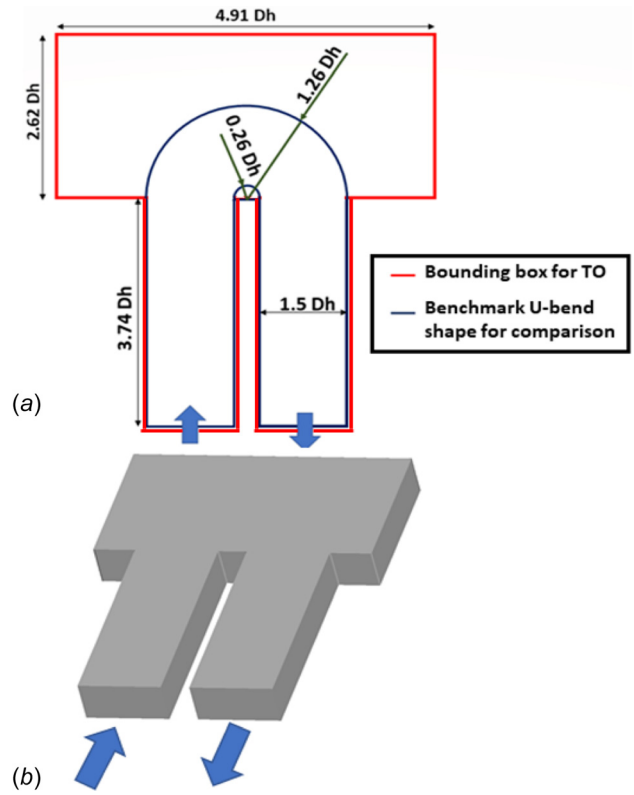

Fig. 5 3D Baseline model of U-bend. TO carried out over the full domain.

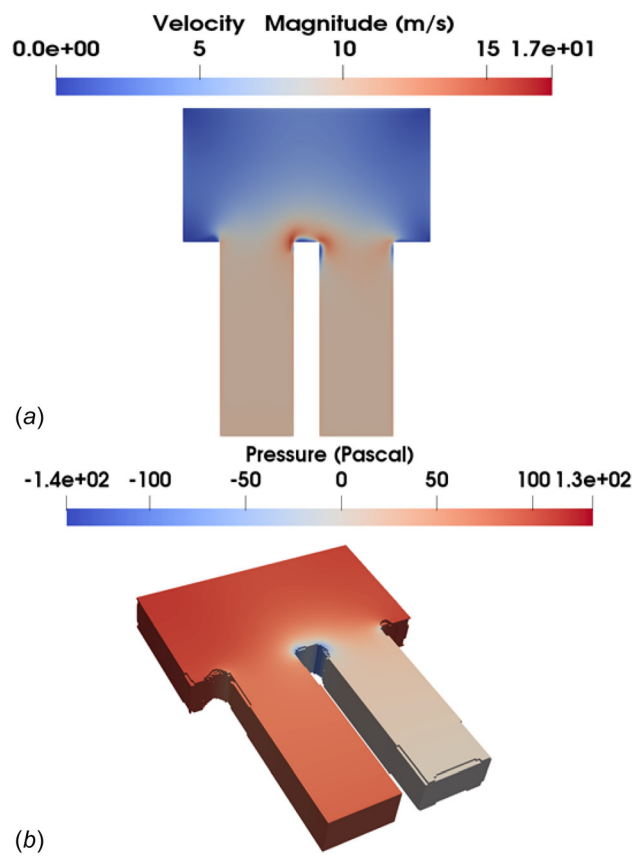

Fig. 6 Velocity magnitude at midplane (*a*) and pressure contours of extracted fluid-path (*b*) for the first optimization step

Downloaded from http://asmedigitalcollection.asme.org/fluidsengineering/article-pdf/144/7/071206/6849053/fe_144_07_071206.pdf by The Pennsylvania State University user on 21 October 2022

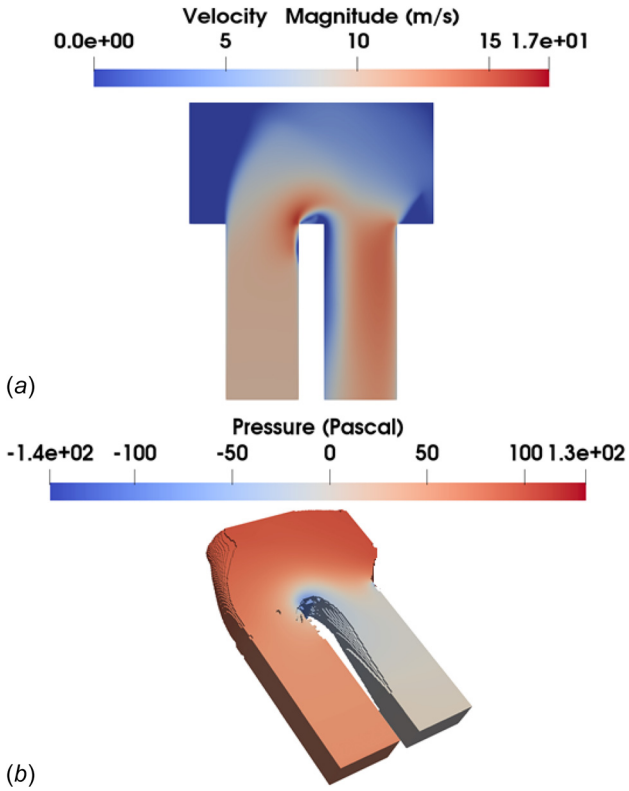

Fig. 7 Velocity magnitude at midplane (*a*) and pressure contours of extracted fluid-path (*b*) for 4000th optimization step

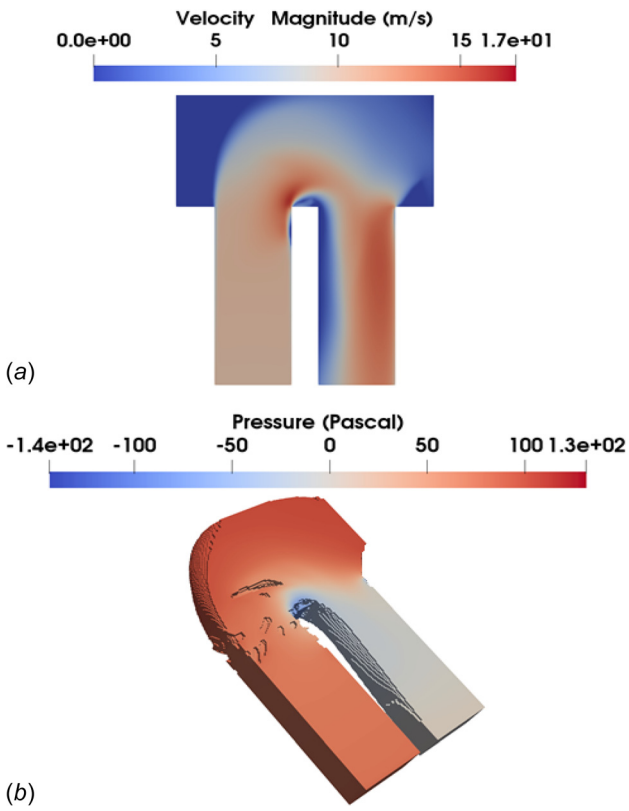

Fig. 8 Velocity magnitude at midplane (*a*) and pressure contours of extracted fluid-path (*b*) for 8000th optimization step

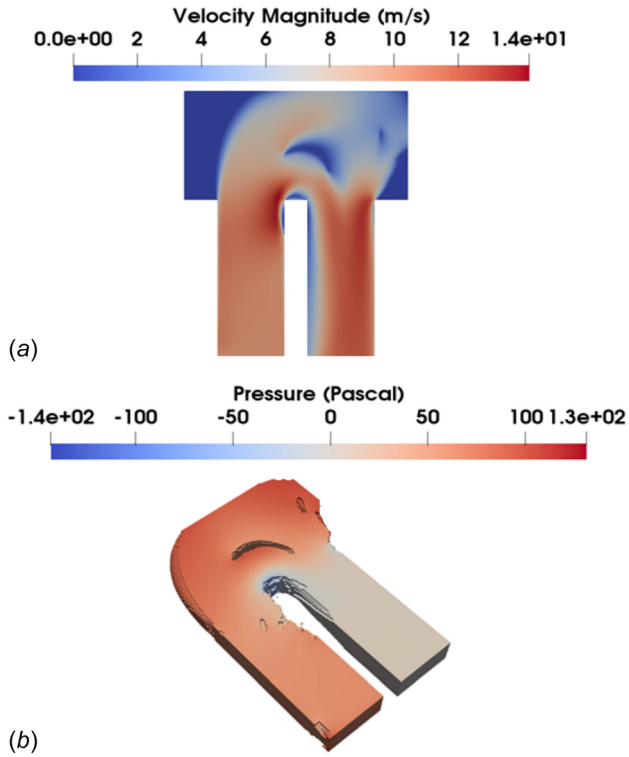

Fig. 9 Velocity magnitude at midplane (*a*) and Pressure contours of extracted fluid-path (*b*) for 12,000th optimization step

without any formations, whereas a number of solid shapes are seen to form near the end-wall by the 4000th iteration (Fig. 11(*c*)). As the iterations progress, one of the solid shapes is seen to grow into a full-fledged vane, while the other smaller shapes disappear at the 10,000th iteration (Fig. 11(*h*)). In other words, the solver decides to get rid of unnecessary blockages which don't aid the objective. The pressure drop is seen to stabilize by the 11,000th iteration. Along with the objective function, the vane growth almost stops in this juncture and stays a constant shape for the rest of the process (Figs. 11(*j*)–11(*l*)). Since the pressure drop value of this benchmark U-bend was obtained from a simulation carried out in STAR-CCM+ with polyhedral mesh and inflation layers, postprocessing and remeshing of this extracted flow path was necessary. This has been documented in the section Simulation in star-ccm+ After Postprocessing Initial TO Results.

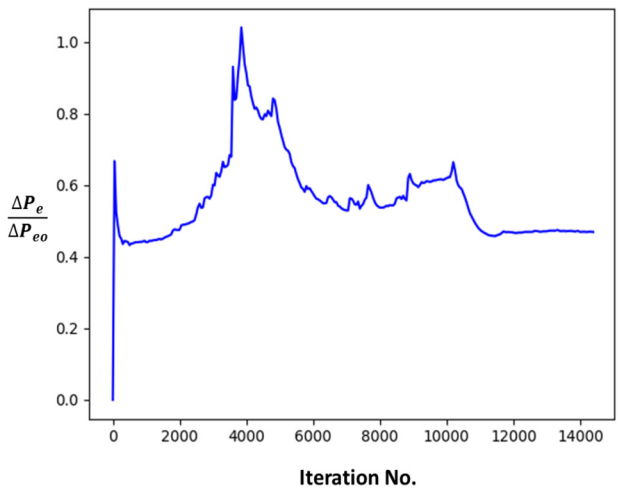

Fig. 10 Pressure drop versus optimization iteration for the entire process

Downloaded from http://asmedigitalcollection.asme.org/fluidsengineering/article-pdf/144/7/071206/6849053/fe_144_07_071206.pdf by The Pennsylvania State University user on 21 October 2022

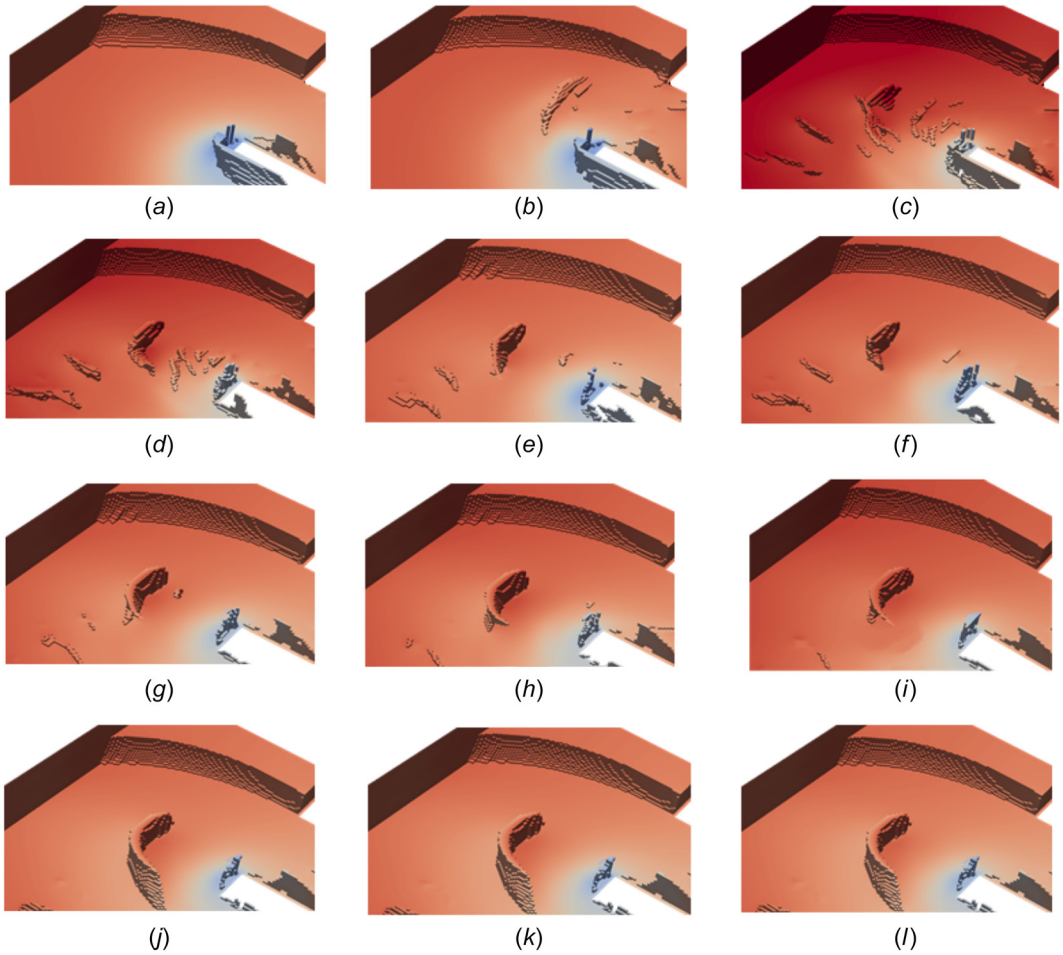

Fig. 11 Zoomed in a half model of U-bend end-wall showing the evolution of turning vane structure at every 1000th iteration starting from (*a*) 2000 to (*l*) 14,000

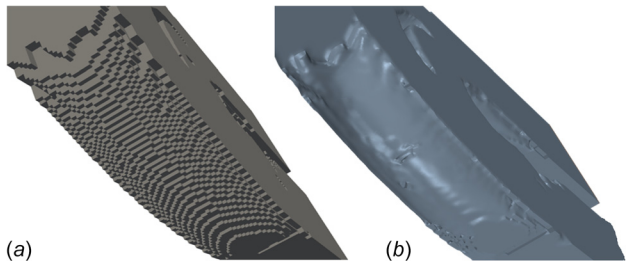

Fig. 12 Side walls (*a*) before and (*b*) after postprocessing and smoothing in STAR-CCM+

Simulation in STAR-CCM+ After Postprocessing Initial TO Results. The exported optimum flow path was found to have rough walls due to the cubic nature of the initial mesh elements. This can be seen as a step like formations in the curved side wall (Fig. 12(*a*)). The surface-repair tool in STAR-CCM+ was used to smooth out similar step-like features throughout the domain while retaining the overall shapes of the boundaries. The final surface (Fig. 13(*a*))was now ready for meshing. A polyhedral mesh with 8 prism layers was used in the STAR-CCM+ automatic polyhedral mesh tool (Fig. 13(*b*)). Final wall $y+$ as a result of the simulation was found to be less than 0.2 (Fig. 13(*c*)). This remeshed simulation was carried out using the realizable k–epsilon turbulence model along with enhanced wall treatment, and identical boundary conditions as the initial TO baseline. Remeshing with inflation layers provides the correct wall treatment to the solid boundaries,

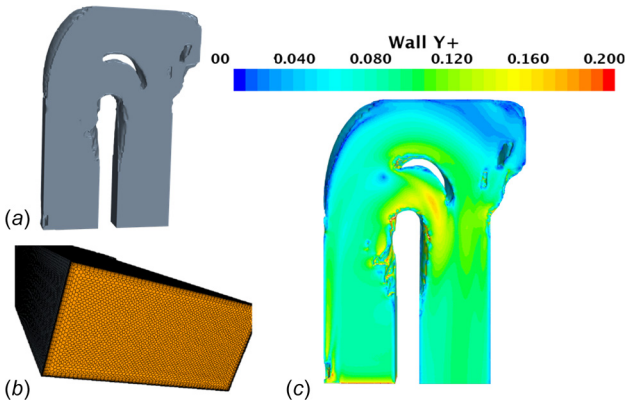

Fig. 13 (*a*) Postprocessed geometry with smoothed shape, (*b*) remeshed in STAR-CCM+ with prism layers for wall-refinement, and (*c*) low wall $y+$ as a result of prism layers

which lacks in the TO scenario. As seen in Table 1, a 3% change in objective function occurs between the raw OPENFOAM case and the postprocessed simulation. Upon confirming the superiority of the TO shape, the 3D printing operation was carried out (Fig. 14) to experimentally test the performance of each channel. Further analysis of the CFD results has been carried out in the section Experimental Tests and Comparison With Computational Fluid Dynamics, with boundary conditions tuned to match the experimental conditions.

Downloaded from http://asmedigitalcollection.asme.org/fluidsengineering/article-pdf/144/7/071206/6849053/fe_144_07_071206.pdf by The Pennsylvania State University user on 21 October 2022

Table 1 Improvement in objective function before and after postprocessing

Case	% pressure drop reduction from benchmark
OPENFOAM TO	53.6
Postprocessed STAR-CCM+	50.3

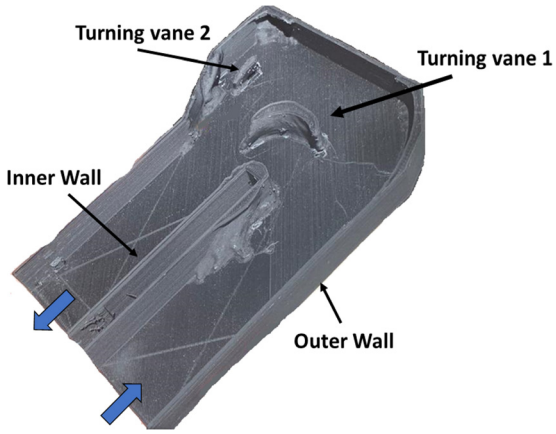

Fig. 14 Midplane cut cross section of 3D printed optimized U-bend channel

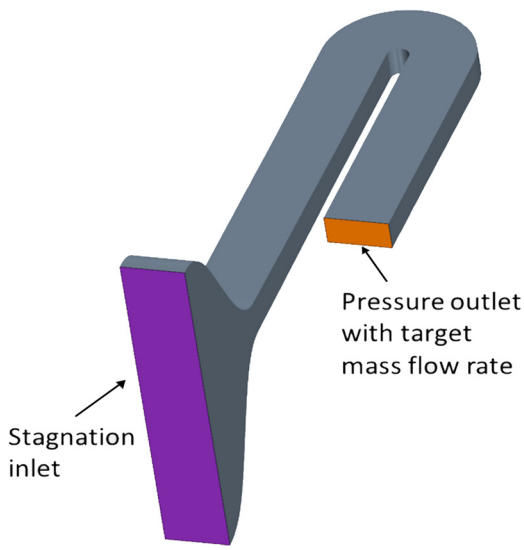

Fig. 15 Modified CFD model for matching experimental conditions

Experimental Tests and Comparison With Computational Fluid Dynamics. The 3D printed benchmark and optimized shapes were assembled into the flow setup (Fig. 4). The CFD model was now modified with an added bell-mouth inlet under suction conditions (Fig. 15), with pressure probes created at the same location as that of the experimental piece (Fig. 16). The mass flow value was adjusted to obtain a velocity of 10 m/s at a probe location in the air-solid, which is identical to the pitot probe location in the experiment. Table 2 documents the objective function augmentations obtained from the experiment and CFD, respectively. The percentage change of pressure reduction between CFD and experimental results was found to be 5%. To understand the reason behind the superior performance of the optimum shape, midplane velocity (Fig. 17) and end-wall pressure contours (Fig. 18) were analyzed. The recirculation region

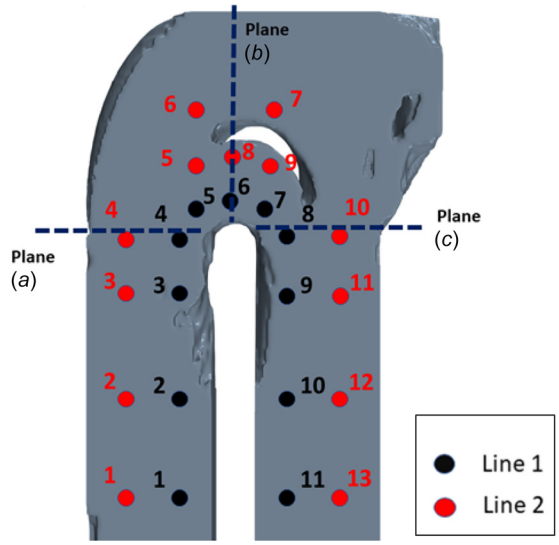

Fig. 16 Tap location for pressure measurements in 3D printed channel

Table 2 Improvement in objective function for experiment and CFD (uncertainty = 6.5%)

Case	% pressure reduction from benchmark
CFD	50.3
Experiment	55

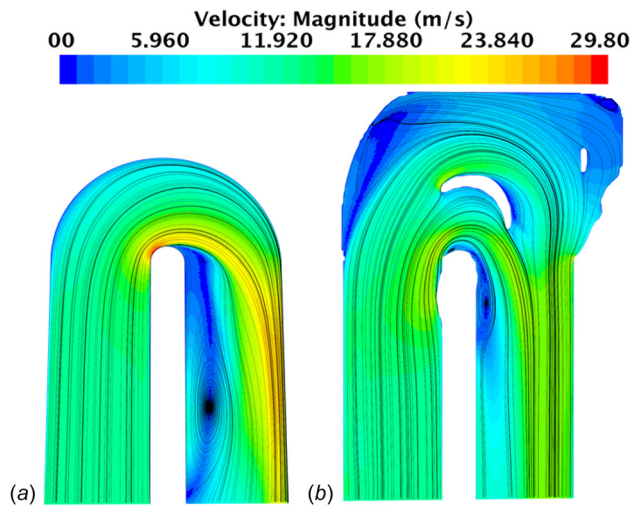

Fig. 17 Midplane velocity profile with streamlines (*a*) benchmark and (*b*) optimum U-bend

downstream of the turn was greatly reduced in the case of the optimum shape when the two geometries are compared (Fig. 17). This recirculation region is formed due to flow separation occurring at the sharp inner wall turn. The turn also causes a radial pressure gradient which is seen to be steeper in the case of the benchmark (Fig. 18). This flow acceleration and separation at the inner wall can also be seen at the cross-sectional view of velocity and secondary flow streamlines (Fig. 19), which shows the counter-rotating Dean vortices. Velocity peaks at the inner wall for the benchmark case signify flow acceleration which eventually leads to a separation bubble visible in the U-bend exit. The separation bubble behaves like a quasi-blockage, which causes the bulk flow

Downloaded from http://asmedigitalcollection.asme.org/fluidsengineering/article-pdf/144/7/071206/6849053/fe_144_07_071206.pdf by The Pennsylvania State University user on 21 October 2022

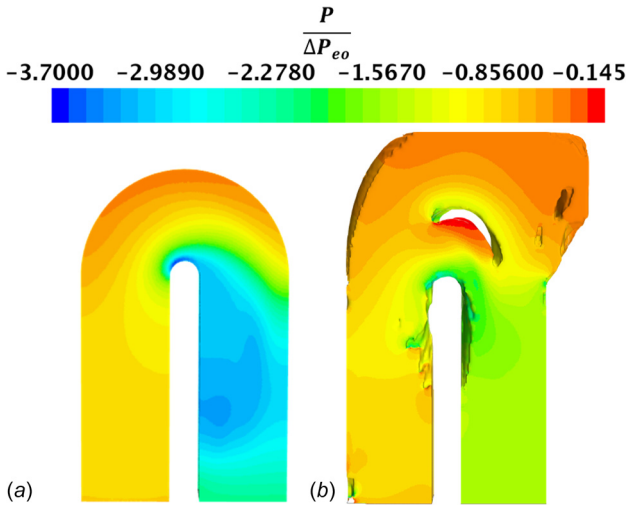

Fig. 18 End-wall pressure profile for (*a*) benchmark and (*b*) optimum U-bend

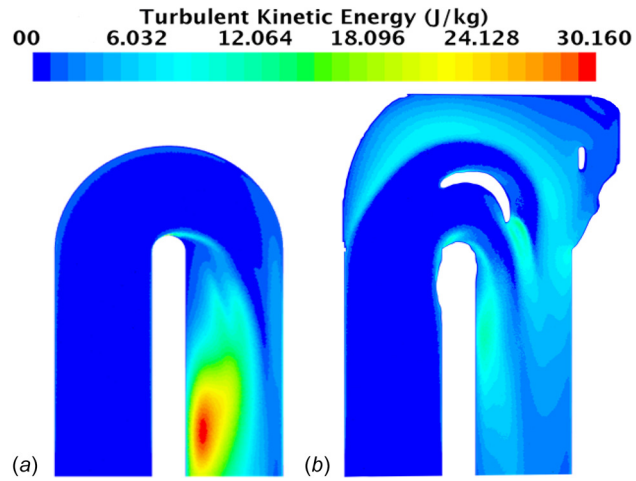

Fig. 20 Midplane TKE contours: (*a*) benchmark and (*b*) optimum

to speed up downstream of the bend and results in high-pressure drop. An impingement effect also occurs on the outer wall near the bend exit due to the acceleration of the flow in a tangential direction to the inner wall at the bend. The expanded duct in case of the optimum shape prevents this impingement effect, and acceleration of the flow at the bend due to contraction of the duct profile at that location helps to suppress the separation bubble. This is in agreement with previous literature which records that presence of turning vanes reduces pressure drop by reducing the strength of secondary flow structures and suppressing turbulent mixing. The midplane TKE plots (Fig. 20) show higher magnitudes in the case of the benchmark shape, which results in higher losses. Furthermore, the turning vane splits up the mass flow at the bend midplane, thereby reducing flow acceleration at the turn by creating a more favorable pressure gradient. The shape of the inner wall of the turning vane also ensures that the accelerated flow near the turn doesn't impinge on the outer wall, thereby directing the flow toward the channel outlet.

Experimental data from the different streamwise pressure tap locations have been plotted for the optimum and benchmark geometry, respectively, in Figs. 21 and 22. For the near inner wall

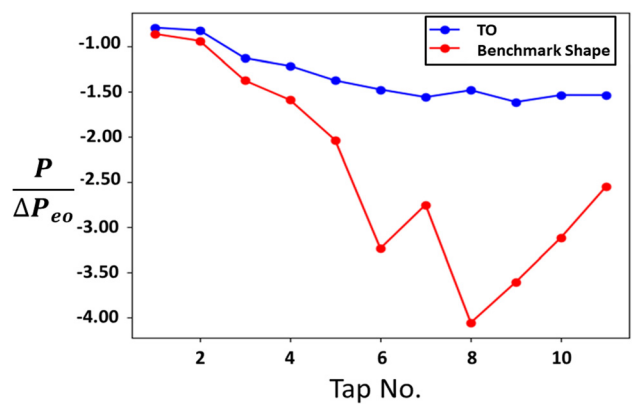

Fig. 21 Streamwise pressure comparison between optimum and benchmark shapes for near inner-wall measurements (Fig. 16, line 1)

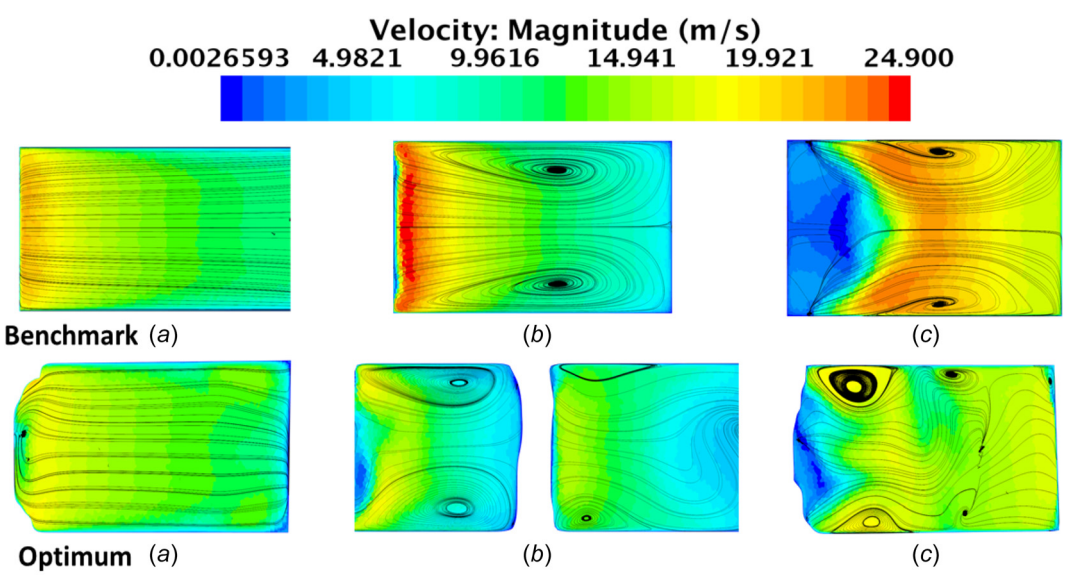

Fig. 19 Velocity magnitudes and secondary stream-lines at three cross-sectional planes as seen in Fig. 16 (inner wall: left, outer wall: right)

Downloaded from http://asmedigitalcollection.asme.org/fluidsengineering/article-pdf/144/7/071206/6849053/fe_144_07_071206.pdf by The Pennsylvania State University user on 21 October 2022

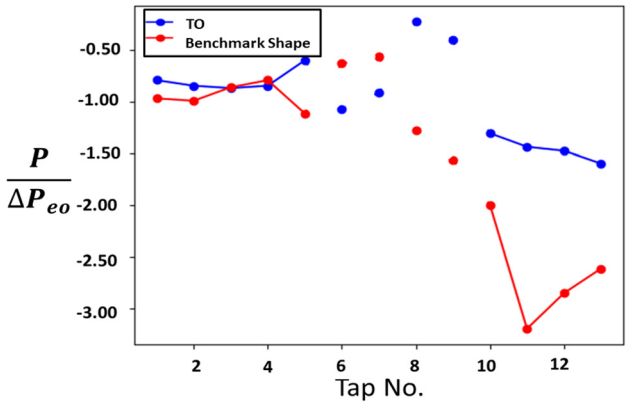

Fig. 22 Streamwise pressure comparison between optimum and benchmark shapes for near outer-wall measurements (Fig. 16, line 2)

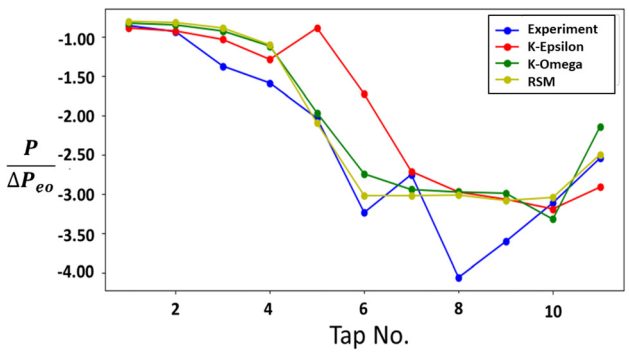

Fig. 23 Streamwise pressure comparison between CFD and experimental data for the benchmark shape near the inner wall (Fig. 16, line 1)

taps (line-1 Fig. 15), a more linear pressure drop is observed in the case of the optimum case. The deviation between the benchmark and TO shape is seen from the fourth tap, which is consistent with the greater flow acceleration for the baseline shape near the inner wall (Fig. 19(*a*)). This trend then continues to a large drop in pressure which occurs at the turn (near tap-6, Fig. 21) for the benchmark case, in close proximity to the flow separation point. Flow acceleration downstream of the turn causes the pressure to keep dropping until it is recovered near the exit due to flow reattachment. This phenomenon is suppressed in the case of the optimum shape, due to the presence of a smaller separation bubble, hence resulting in a more linear pressure drop profile. Effect of the separation bubble is also seen in the tap locations near the outer wall of the benchmark case(line-2, Fig. 16), where a sudden drop in pressure is observed at the downstream of the turn (tap 10, 11; Fig. 22) due to impingement of accelerated flow on the outer wall. Besides this sudden drop, the pressure profiles at the outer wall are almost similar for the two shapes. The presence of two small packets of recirculation at the upper left and right corners outer wall of the optimum shape (Fig. 17) doesn't appear to contribute greatly to the overall pressure drop when compared to the benchmark.

Three different turbulence models were used to compare streamwise pressure drop data with experimental cases (Figs. 23–26). This helped evaluate the performance of two-equation models like k–ω SST, k–ϵ, and RSM models against the experimental case. For the benchmark shape, all the turbulence models fail to catch the minimum pressure point for the near inner wall taps, compared to the experiment (Fig. 23, point 8), with the k–ϵ model performing the worst. However, the overall trend and exit pressure are predicted closely by all the models. This can be

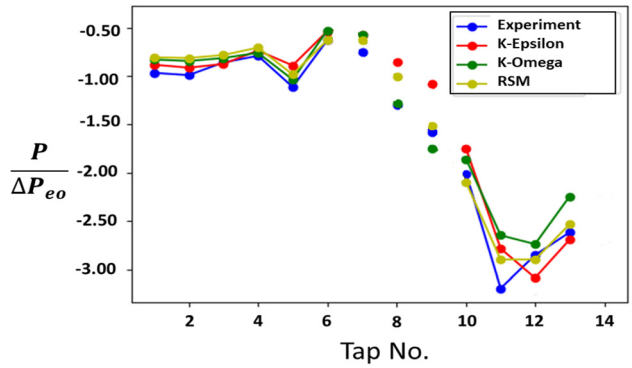

Fig. 24 Streamwise pressure comparison between CFD and experimental data for the benchmark shape near the outer wall (Fig. 16, line 2)

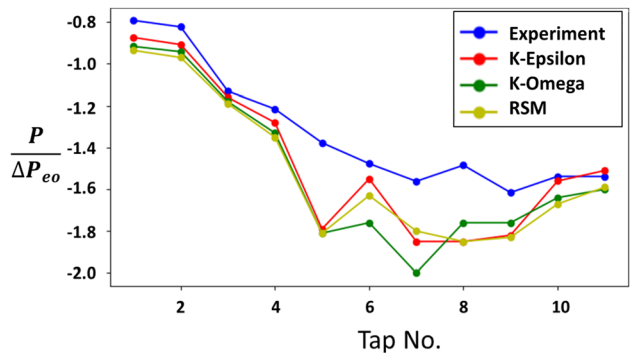

Fig. 25 Streamwise pressure comparison between CFD and experimental data for the optimum shape near the inner wall (Fig. 16, line 1)

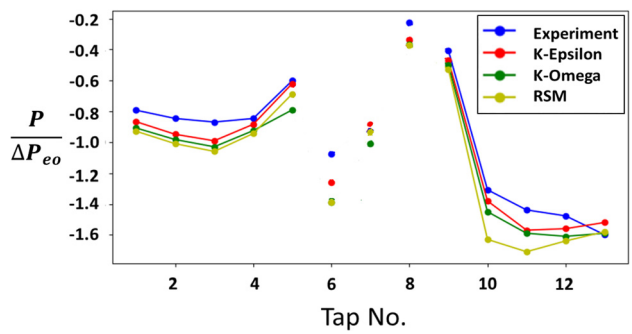

Fig. 26 Streamwise pressure comparison between CFD and experimental data for the optimum shape near the outer wall (Fig. 16, line 2)

attributed to the under-prediction of the separation bubble size, which also under-predicts the magnitude of flow acceleration downstream of the bend, thereby resulting in a lower magnitude of local pressure drop. The opposite is seen in the case of the optimum geometry, where the lowest pressure drop is over-predicted for the near inner-wall measurements (Fig. 15), with the k–ϵ model having the closet prediction. For both the shapes, pressure measurements near the outer walls (Figs. 24 and 26) were accurately predicted by all the CFD models due to the lack of major flow separation at these locations. Due to the underprediction of the separation bubble size at the inner wall, the minimum pressure magnitude at the near-outer wall taps for the benchmark case (Fig. 24, point 11) was also underpredicted by the CFD models.

Downloaded from http://asmedigitalcollection.asme.org/fluidsengineering/article-pdf/144/7/071206/6849053/fe_144_07_071206.pdf by The Pennsylvania State University user on 21 October 2022

Comparison With Parametric Optimization Methods. As a relatively newer method of optimization, compared to pre-existing parametric schemes which use multiple simulated data points to arrive at a global optimum, it is important to compare the performance of TO with parametric methods for similar geometries. In the section Parametric Shape Optimization Using Surrogate Model-Based Bayesian Method, the TO case is compared to experimental and numerical results of an in-house parametric study using surrogate model Bayesian optimization and the study by Verstraete et al. [12] and Colletti et al. [13], which are also performed against the same benchmark U-bend.

Parametric Shape Optimization Using Surrogate Model-Based Bayesian Method. Similar to the approach used by Verstraete et al. [12], the U-bend shape was parametrized within a given bounding box using spline curves governed by control points. Two spline curves were used as the inner and outer walls of the U-bend shape. These curves are governed by the position of control points. Changing the spatial positions (co-ordinates) of the control points resulted in the morphing of the spline curves (Fig. 27). The shorter inner spline had three control points, while the larger outer spline had five. Subsequently, a 2D design space was created by varying the x and y coordinates of the eight control points within a bounding box (shown in Fig. 27). This 16-dimensional design space has been explained in detail in Fig. 28. This design space was used for an initial Latin Hypercube Sampling [44]. Each design point in these samples was a combination of the 16 design parameters which were then fed into a scripted computer aided design interface in ANSYS SPACECLAIM to create a unique design.

Sixty initial simulations were run to train the surrogate model with the pressure drop as the objective function. A search space of 1000 points was created following the initial training. Using the expected improvement function peaks, Bayesian updates were sampled. Due to the exploration versus exploitation nature of this sampling, unexplored (high uncertainty) regions, as well as low objective function designs were searched for. A sampling at the high-uncertainty regions, in addition to the low-uncertainty regions with favorable objective function values, accounts for the chances of the presence of a global optimum at the relatively unknown regions of the black-box function. This process has been summarized by a flowchart in Fig. 29. The design of experiments (DoE) points can be seen in iterations 1-60 (Fig. 30), along with the Bayesian update points from 60-85. Normalized bend pressure drop values are seen to drop below 1 for most of the optimization points, with the lowest value for the optimum point visible in the last iteration in Fig. 30. Detailed description and mathematical background of this method can be found in Ghosh et al. [40,41]. Each CFD simulation in STAR-CCM+ approximately took 2 h to complete in a PC with a six core intel core i7 processor (when run in parallel). The total computation budget was around 170 h for 60 initial design points and 25 optimization iterations. Identical mesh parameters and boundary conditions were used as the benchmark case.

The optimum shape obtained from Bayesian optimization (BO), shows a rounded inner wall, with an expansion in the shape of the duct due to the outward curvature of the outer wall (Fig. 31(*a*)). A

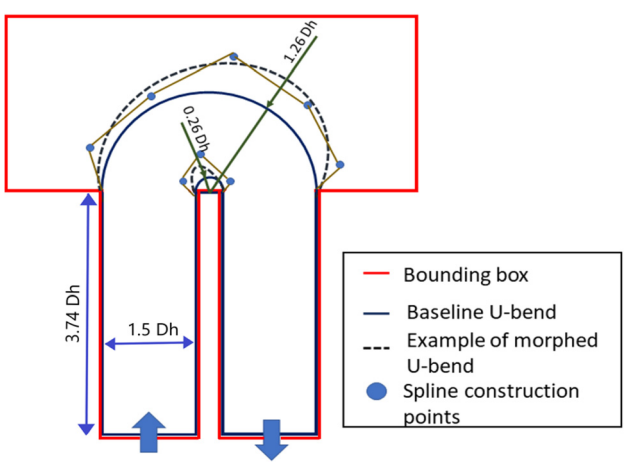

Fig. 27 Parametrization of baseline design using splines

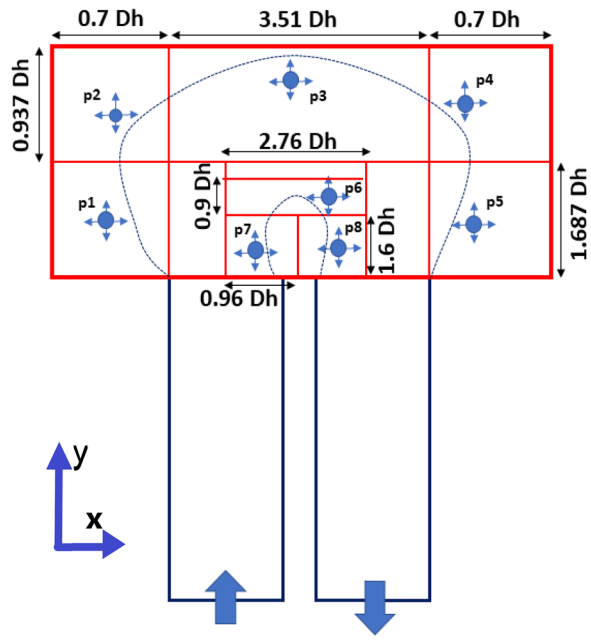

Fig. 28 Design domains for spline control points. Variation of control point coordinates within given bounds creates unique spline curves.

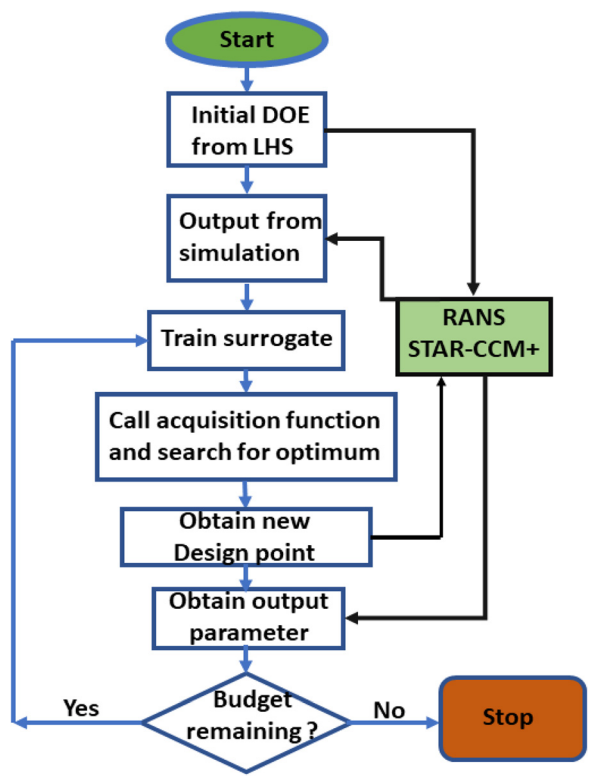

Fig. 29 Flowchart explaining surrogate model-based Bayesian optimization

Downloaded from http://asmedigitalcollection.asme.org/fluidsengineering/article-pdf/144/7/071206/6849053/fe_144_07_071206.pdf by The Pennsylvania State University user on 21 October 2022

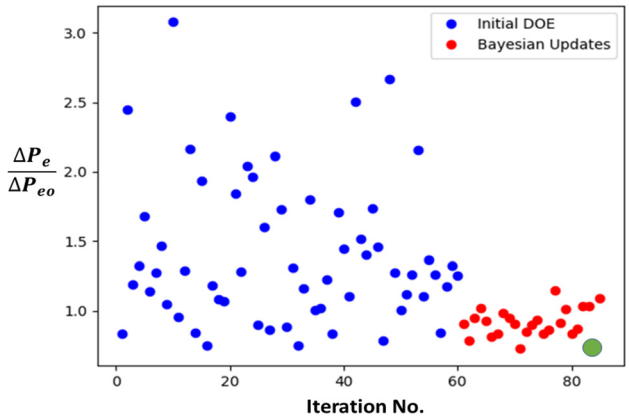

Fig. 30 DoE and Bayesian updates for the design optimization process (optimum design point in last iteration.)

comparison of midplane velocity contours (Fig. 31) shows the formation of a bigger separation bubble for the Bayesian shape optimized case. The Bayesian optimized geometry shows a smaller bubble compared to the benchmark, but the absence of vanes fails to control the acceleration of flow around the midbend. Flow-streamlines also show a curvature toward the outer wall to a larger extent when compared to the TO shape. This creates a larger bubble compared to the TO shape, and a higher local acceleration of flow around the bend exit along with flow-impingement on the outer wall. The end-wall pressure contours (Fig. 32) show steep gradients for both the shapes near the inner wall of the U-bends, but a larger area of steep pressure gradients is observed for the BO shape, which coincides with the location of the flow-separation and recirculation zone. A 3D printed shape was created from the CFD design optimization process (Fig. 33) for the BO case, for experimental validation purposes. The observations from experimental measurements (Figs. 34 and 35) reflect those of the earlier findings from CFD. For the near inner wall streamwise pressure measurements, a bigger drop in pressure was noticed at the midbend region for the BO shape (Fig. 25, point 7) owing to flow acceleration, compared to the more linear pressure drop for the TO shape. Similarly, for the near outer wall region (Fig. 35), a bigger pressure peak is seen for points 6–9, which are on the convex side of the airfoil like turning vane of the TO geometry. A sharp drop is seen at the outer bend exit region of the BO shape (points 10–11), due to the impinging effect of the accelerating flow due to the presence of a larger recirculation bubble, similar to the benchmark shape, but lower in magnitude. The BO and TO

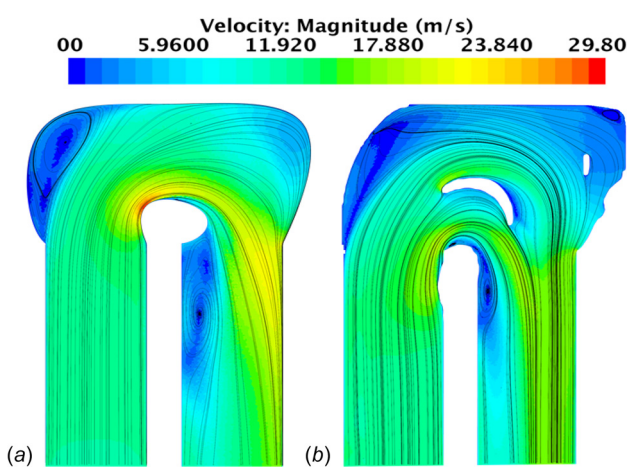

Fig. 31 Midplane velocity contours and streamlines for: (*a*) Bayesian shape optimized channel and (*b*) TO shape

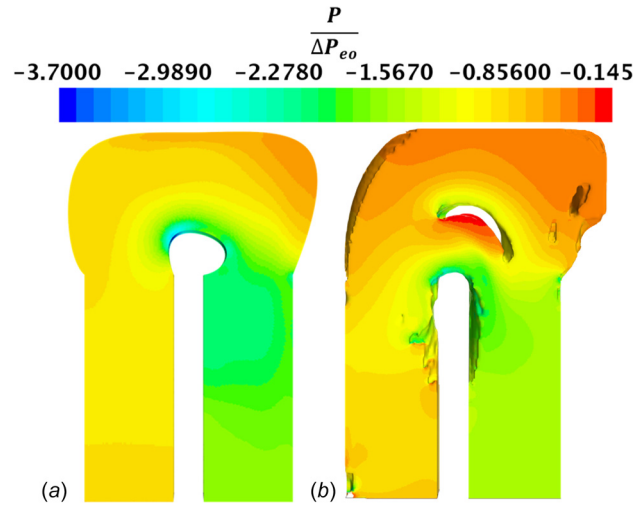

Fig. 32 End-wall pressure contours for: (*a*) Bayesian shape optimized channel and (*b*) TO shape

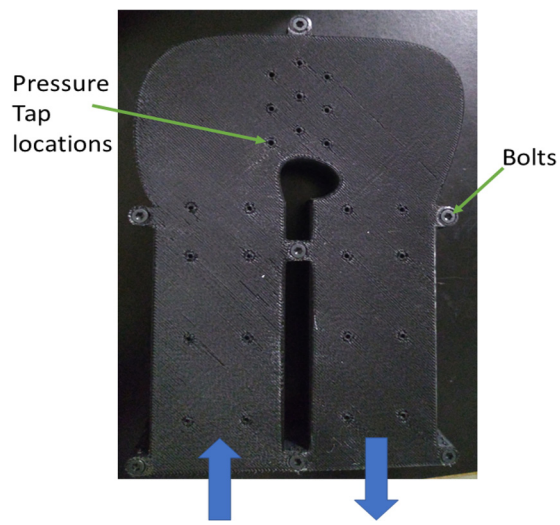

Fig. 33 3D printed U-bend channel from Bayesian shape optimization

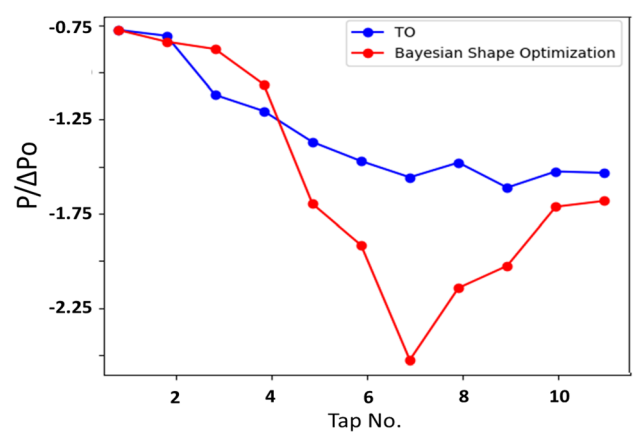

Fig. 34 Experimental streamwise pressure measurements for TO and Bayesian optimization geometries (line-1, 16)

Downloaded from http://asmedigitalcollection.asme.org/fluidsengineering/article-pdf/144/7/071206/6849053/fe_144_07_071206.pdf by The Pennsylvania State University user on 21 October 2022

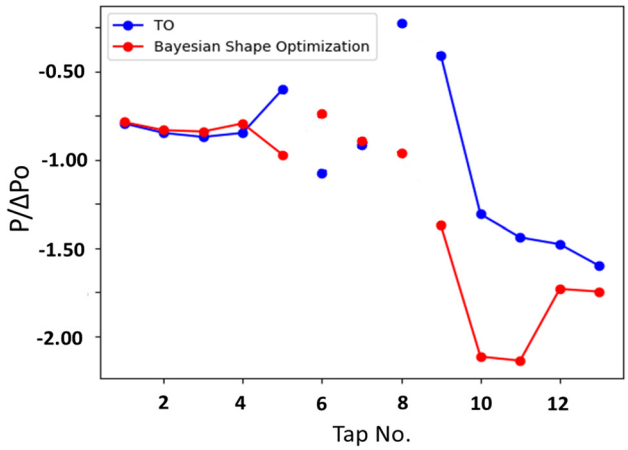

Fig. 35 Experimental streamwise pressure measurements for TO and Bayesian optimization geometries (line-2, 16)

methodologies are fundamentally different, and the manual bias involved behind the choice of design points in the parametric study has also influenced the pressure drop performance in the BO optimum. (This can explain the difference between the Verstraete et al. [12] case and the BO performance from this study in Table 3). No such bias however is present in the TO case, and the computation time is lower as well.

Heat Transfer and Thermal Performance Efficiency. Heat transfer results were calculated to make sure the optimization process did not have adverse effects on the thermal performance of the channel. The formerly adiabatic end-walls in previous simulations were now changed to heated walls with a temperature of 350 K, with inlet fluid temperature of 300 K. Inbuilt definition of Nusselt number was used to evaluate heat transfer from forced convection for the two optimized shapes, as well as the benchmark channel

$$\mathrm{Nu} = \frac{hD_h}{k} \tag{18}$$

where convective heat transfer coefficient h is defined in STAR-CCM+ as

$$h = \frac{\rho(y_c)C_p u_\tau}{T^+ y^+} \tag{19}$$

where $y^+ = u_\tau y_c/\nu$, $y_c =$ cell centroid distance from the wall for the first cell, friction velocity $u_\tau = \tau/\rho$ and $T^+ = Pry^+$. A wall y^+ of 100 has been used as suggested by the STAR-CCM+ manual. End-wall Nusselt number comparisons have been shown in Fig. 36. Low magnitudes regions of Nu can be seen for the benchmark and BO cases downstream of the U-bend, which coincides with the separation regions in those cases and is absent in the case of the TO shape. For the benchmark case, a high heat transfer region can be seen (in yellow) alongside the separation regions due to the acceleration of the fluid. Similar high magnitude regions of Nu can be seen for the TO case just below the bigger turning vane, where a peak is achieved at the stagnation point. Near wall TKE contours (Fig. 37) show higher magnitude peaks for the benchmark case when compared to the optimum shapes.

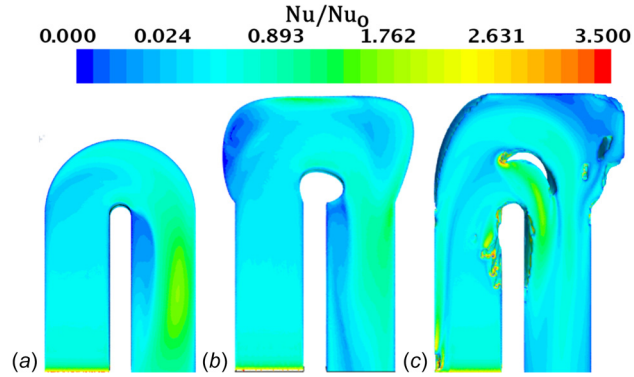

Fig. 36 End-wall normalized Nusselt number contours for the benchmark (*a*), BO (*b*), and TO (*c*)

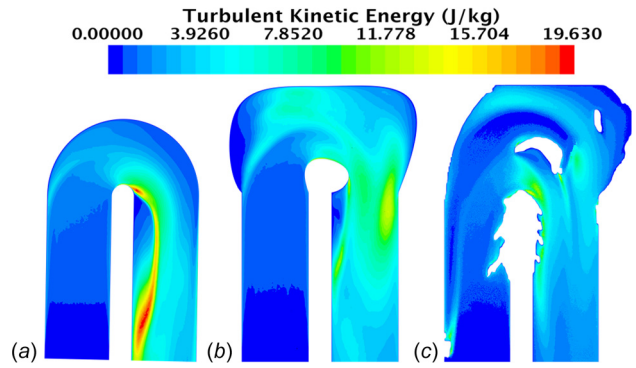

Fig. 37 Near-wall TKE contours (0.2 mm from wall) for the benchmark (*a*) BO (*b*) and TO (*c*)

Table 4 Comparison between average Nusselt number and thermal performance efficiency η for the two optimization approaches

Case	Nu/Nu$_o$	% improvement in η from benchmark
TO	0.96	20
BO	0.94	12

The high TKE magnitude regions for all cases are located in the shear layer beside the separation bubble at the bend exit and the inner wall at midbend. Due to a larger recirculation bubble, the biggest TKE peaks can be seen in red for the benchmark U-bend. A TKE peak is also seen near the outer wall, downstream of the shape for the BO shape. This is due to the impinging flow near the wall (Fig. 31), which is eliminated due to the presence of a turning vane in the case of the TO shape.

Thermal performance efficiency (η) helps to understand the lumped effect of heat transfer and pressure drop

$$\eta = (\mathrm{Nu}/\mathrm{Nu}_o)/(f/f_o)^{1/3} \tag{20}$$

Table 3 Comparison between CFD and experimental pressure drop in two different approaches

Case	CFD	Experiment	% degree of freedom	No. of iterations simulated	Hours
TO	50.3	55	1 Mil	2 (TO)+1	15 + 2
BO	30	35	16	85	170
Refs. [12] and [13]	37.6	36	26	85 (Kriging)	170

Experimental uncertainty of 6.5%.

Downloaded from http://asmedigitalcollection.asme.org/fluidsengineering/article-pdf/144/7/071206/6849053/fe_144_07_071206.pdf by The Pennsylvania State University user on 21 October 2022

where friction factor f

$$f = \frac{\Delta P}{\frac{1}{2}\rho v^2} \tag{21}$$

Table 4 shows that although the average end-wall Nusselt numbers of the TO and Bayesian parametric optimum shapes fall by 4% and 6%, respectively, η for both the shapes are better by 20% and 12% compared to the benchmark. The more turbulent flow in the case of the benchmark results in higher end-wall Nu peaks, but the low heat transfer flow separated regions end up reducing the overall average Nu. The reduction of the pressure drop for the optimum shapes, on the other hand, improves the overall efficiency of the heat exchanger geometries, with the TO outperforming the parametric optimization approach.

Conclusions

A topology optimization method has been used to optimize the flow-path in a U-bend channel for pressure drop minimization. U-bends are an integral part of serpentine cooling channels which are employed in gas turbine blade cooling and other industrial applications. Reducing pressure drop can improve thermal performance efficiency, in turn improving the thermodynamic cycle efficiency. The TO shape showed an improvement of 53% compared to a benchmark U-bend used in literature. A smoothed, post-processed geometry was created after extracting the flow-path from the initial TO case for remeshing and simulating in STAR-CCM+. This simulation showed a 3% deviation from the unsmoothed case. The TO shape showed a rounded inner wall turn along with the formation of two turning vanes near the mid-bend and downstream region of the U-bend. The recirculation zone formed downstream of the bend was reduced for the TO case, due to a reduction in the adverse gradient at the turn radius region. Experimental studies were carried out using 3D printed acrylonitrile butadiene styrene geometries of the TO and benchmark shapes, where a 5% difference was seen from CFD cases. Eddy viscosity models and RSM models were found to correctly predict overall trends and pressure drops, despite local deviations near flow separation regions. Comparison of the TO shape with an in-house parametrized shape optimization and another case from the literature showed an objective function improvement of 14%, which equated to a higher thermal performance efficiency by 8%. A higher degree-of-freedom resulted in a more unconventional shape in the case of the TO, and a number of iterations required to arrive at an optimum was found to be significantly smaller for the TO case since a single TO optimization iteration is equivalent to two regular RANS simulations.

Funding Data

- Florida Makes (Award No. 70NANB15H041).
- Florida High Tech Corridor Programs (Award No. AWD00000135).

Nomenclature

C_1, C_2, C_3 and C C_μ = k–ϵ model constants
CFD = computational fluid dynamics
D_h = hydraulic diamater of U-bend channel
D_k = diffusivity rate for TKE
D_ϵ = diffusivity rate for turbulent dissipation
h = convection heat transfer coefficient
NS = Navier–Stokes equation
Nu = Nusselt number
Nu_o = Nusselt number baseline
p = static pressure
p_a = adjoint pressure
R_1 = momentum constraint
R_2 = continuity constraint
T_{wall} = wall surface temperature
T^+ = nondimensional temperature
TO = topology optimization
TKE = turbulent kinetic energy
u = primal velocity
u_a = adjoint velocity
u_{an} = normal component of adjoint velocity
u_n = normal component of primal velocity
u_τ = friction velocity
wall y^+ = nondimensional wall distance
y_c = cell centroid distance from wall for the first cell
α = Brinkman penalty term
α_{Max} = Brinkman penalty term maximum value
γ = fluid fraction
ΔP_e = pressure drop across the channel
ΔP_{eo} = baseline pressure drop
ρ = density

References

[1] Bunker, R. S., 2017, "Evolution of Turbine Cooling," ASME Paper No. GT2017-63205.
[2] Dean, W. R., 1927, "Xvi. Note on the Motion of Fluid in a Curved Pipe," London, Edinburgh, Dublin Philos. Mag. J. Sci., **4**(20), pp. 208–223.
[3] Metzger, D. E., Plevich, C. W., and Fan, C. S., 1984, "Pressure Loss Through Sharp 180 Deg Turns in Smooth Rectangular Channels," ASME J. Eng. Gas Turbines Power, **106**(3), pp. 677–681.
[4] Son, S., Kihm, K., and Han, J.-C., 2002, "PIV Flow Measurements for Heat Transfer Characterization in Two-Pass Square Channels With Smooth and 90° Ribbed Walls," Int. J. Heat Mass Transfer, **45**(24), pp. 4809–4822.
[5] Liou, T.-M., Tzeng, Y.-Y., and Chen, C.-C., 1999, "Fluid Flow in a 180 Deg Sharp Turning Duct With Different Divider Thicknesses," ASME J. Turbomach., **121**(3), pp. 569–576.
[6] Chu, H.-C., Chen, H.-C., and Han, J.-C., 2018, "Numerical Simulation of Flow and Heat Transfer in Rotating Cooling Passage With Turning Vane in Hub Region," ASME J. Heat Transfer-Trans. ASME, **140**(2), p. 021701.
[7] Schüler, M., Zehnder, F., Weigand, B., von Wolfersdorf, J., and Neumann, S. O., 2011, "The Effect of Turning Vanes on Pressure Loss and Heat Transfer of a Ribbed Rectangular Two-Pass Internal Cooling Channel," ASME J. Turbomach., **133**(2), p. 021017.
[8] Valsala, R. R., Son, S., Suryan, A., and Kim, H. D., 2019, "Study on Reduction in Pressure Losses in Pipe Bends Using Guide Vanes," J. Visual., **22**(4), pp. 795–807.
[9] Sleiti, A. K., and Kapat, J. S., 2004, "Comparison Between EVM and RSM Turbulence Models in Predicting Flow and Heat Transfer in Rib-Roughened Channels," Parts A and B of Heat Transfer Summer Conference, Volume 2, pp. 531–542.
[10] Sewall, E. A., and Tafti, D. K., 2005, "Large Eddy Simulation of Flow and Heat Transfer in the 180° Bend Region of a Stationary Ribbed Gas Turbine Internal Cooling Duct," Parts A and B of Turbo Expo: Power for Land, Sea, and Air, Volume **3**: Turbo Expo, Reno, NV, pp. 481–493.
[11] Otto, M., Hodges, J., Gupta, G., and Kapat, J. S., "Vortical Structures in Pin Fin Arrays for Turbine Cooling Applications," ASME Paper No. GT2019-90552.
[12] Verstraete, T., Coletti, F., Bulle, J., Vanderwielen, T., and Arts, T., 2013, "Optimization of a U-Bend for Minimal Pressure Loss in Internal Cooling Channels-Part I: Numerical Method," ASME J. Turbomach., **135**(5), p. 051015.
[13] Coletti, F., Verstraete, T., Bulle, J., Van der Wielen, T., Van den Berge, N., and Arts, T., 2013, "Optimization of a U-Bend for Minimal Pressure Loss in Internal Cooling Channels-Part II: Experimental Validation," ASME J. Turbomach., **135**(5), p. 051016.
[14] Ghosh, S., and Kapat, J. S., 2019, "Topology Optimization of Serpentine Channels for Minimization of Pressure Loss and Maximization of Heat Transfer Performance as Applied for Additive Manufacturing," Heat Transfer of Turbo Expo: Power for Land, Sea, and Air, Volume **5B**, Phoenix, AZ.
[15] Dilgen, S. B., Dilgen, C. B., Fuhrman, D. R., Sigmund, O., and Lazarov, B. S., 2018, "Density Based Topology Optimization of Turbulent Flow Heat Transfer Systems," Struct. Multidiscip. Optim., **57**(5), pp. 1905–1918.
[16] Bendsøe, M. P., and Kikuchi, N., 1988, "Generating Optimal Topologies in Structural Design Using a Homogenization Method," Comput. Methods Appl. Mech. Eng., **71**(2), pp. 197–224.
[17] Dbouk, T., 2017, "A Review About the Engineering Design of Optimal Heat Transfer Systems Using Topology Optimization," Appl. Therm. Eng., **112**, pp. 841–854.
[18] Alexandersen, J., and Andreasen, C., 2020, "A Review of Topology Optimisation for Fluid-Based Problems," Fluids, **5**(1), p. 29.
[19] Borrvall, T., and Petersson, J., 2003, "Topology Optimization of Fluids in Stokes Flow," Int. J. Numer. Methods Fluids, **41**(1), pp. 77–107.
[20] Gersborg-Hansen, A., Sigmund, O., and Haber, R., 2005, "Topology Optimization of Channel Flow Problems," Struct. Multidiscip. Optim., **30**(3), pp. 181–192.

Downloaded from http://asmedigitalcollection.asme.org/fluidsengineering/article-pdf/144/7/071206/6849053/fe_144_07_071206.pdf by The Pennsylvania State University user on 21 October 2022

[21] Wiker, N., Klarbring, A., and Borrvall, T., 2007, "Topology Optimization of Regions of Darcy and Stokes Flow," Int. J. Numer. Methods Eng., **69**(7), pp. 1374–1404.
[22] Guest, J. K., and Smith Genut, L. C., 2010, "Reducing Dimensionality in Topology Optimization Using Adaptive Design Variable Fields," Int. J. Numer. Methods Eng., **81**(8), pp. 1019–1045.
[23] Bruns, T., 2007, "Topology Optimization by Penalty (Top) Method," Comput. Methods Appl. Mech. Eng., **196**(45–48), pp. 4430–4443.
[24] Yaji, K., Yamada, T., Yoshino, M., Matsumoto, T., Izui, K., and Nishiwaki, S., 2014, "Topology Optimization Using the Lattice Boltzmann Method Incorporating Level Set Boundary Expressions," J. Comput. Phys., **274**, pp. 158–181.
[25] Zhou, S., and Li, Q., 2008, "A Variational Level Set Method for the Topology Optimization of Steady-State Navier–Stokes Flow," J. Comput. Phys., **227**(24), pp. 10178–10195.
[26] Challis, V. J., and Guest, J. K., 2009, "Level Set Topology Optimization of Fluids in Stokes Flow," Int. J. Numer. Methods Eng., **79**(10), pp. 1284–1308.
[27] Yoshimura, M., Shimoyama, K., Misaka, T., and Obayashi, S., 2017, "Topology Optimization of Fluid Problems Using Genetic Algorithm Assisted by the Kriging Model," Int. J. Numer. Methods Eng., **109**(4), pp. 514–532.
[28] Othmer, C., 2008, "A Continuous Adjoint Formulation for the Computation of Topological and Surface Sensitivities of Ducted Flows," Int. J. Numer. Methods Fluids, **58**(8), pp. 861–877.
[29] Ghosh, S., and Kapat, J. S., 2020, "Topology Optimization of High Aspect Ratio Internal Cooling Channels as a Design for Additive Manufacturing," Volume 7A: Heat Transfer Turbo Expo: Power Land, Sea, Air, London, UK.
[30] Pietropaoli, M., Ahlfeld, R., Montomoli, F., Ciani, A., and D'Ercole, M., 2017, "Design for Additive Manufacturing: Internal Channel Optimization," ASME J. Eng. Gas Turbines Power, **139**(10), p. 102101.
[31] Kontoleontos, E., Papoutsis-Kiachagias, E., Zymaris, A., Papadimitriou, D., and Giannakoglou, K., 2013, "Adjoint-Based Constrained Topology Optimization for Viscous Flows, Including Heat Transfer," Eng. Optim., **45**(8), pp. 941–961.
[32] Philippi, B., and Jin, Y., 2015, "Topology Optimization of Turbulent Fluid Flow With a Sensitive Porosity Adjoint Method (Spam)," arXiv preprint arXiv:1512.08445.
[33] Jin, Y., Uth, M., Kuznetsov, A., and Herwig, H., 2015, "Numerical Investigation of the Possibility of Macroscopic Turbulence in Porous Media: A Direct Numerical Simulation Study," J. Fluid Mech., **766**, pp. 76–103.
[34] Dede, E. M., Joshi, S. N., and Zhou, F., 2015, "Topology Optimization, Additive Layer Manufacturing, and Experimental Testing of an Air-Cooled Heat Sink," ASME J. Mech. Des., **137**(11), p. 111403.
[35] Ruiz, A., Fezzaa, K., Kapat, J., and Bhattacharya, S., 2020, "Measurements of the Flow in the Vicinity of an Additively Manufactured Turbine Leading-Edge Using x-Ray Particle Tracking Velocimetry," ASME J. Fluids Eng., **142**(5), p. 051502.
[36] Calderon, L., Curbelo, A., Gupta, G., and Kapat, J. S., 2018, "Adiabatic Film Cooling Effectiveness of a Lam Fabricated Porous Leading Edge Segment of a Turbine Blade," ASME Paper No. GT2018-77114.
[37] Liu, C., Guo, M., Yan, Q., Wei, W., and Wood, H. G., 2020, "Parametric Analysis and Optimization of Leaning Angle in Torque Converters," ASME J. Fluids Eng., **142**(10), p. 101208.
[38] Maral, H., Şenel, C. B., Deveci, K., Alpman, E., Kavurmacıoğlu, L., and Camci, C., 2020, "A Genetic Algorithm Based Multi-Objective Optimization of Squealer Tip Geometry in Axial Flow Turbines: A Constant Tip Gap Approach," ASME J. Fluids Eng., **142**(2), p. 021402.
[39] Iliev, I., Tengs, E. O., Trivedi, C., and Dahlhaug, O. G., 2020, "Optimization of Francis Turbines for Variable Speed Operation Using Surrogate Modeling Approach," ASME J. Fluids Eng., **142**(10), p. 101214.
[40] Ghosh, S., Mondal, S., Fernandez, E., Kapat, J. S., and Roy, A., 2020, "Parametric Shape Optimization of Pin-Fin Arrays Using a Surrogate Model-Based Bayesian Method," J. Thermophys. Heat Transfer, **35**, pp. 1–11.
[41] Ghosh, S., Mondal, S., Fernandez, E., Kapat, J. S., and Roy, A., 2020, "Shape Optimization of Pin Fin Arrays Using Gaussian Process Surrogate Models Under Design Constraints," ASME Paper No. GT2020-15277.
[42] Patankar, S., 2018, *Numerical Heat Transfer and Fluid Flow*, CRC Press, Boca Raton, FL.
[43] Bell, J. H., and Mehta, R. D., 1988, "Contraction Design for Small Low-Speed Wind Tunnels," NASA STI/Recon, Stanford University, Stanford, CA, Report No. JIAA TR-84.
[44] McKay, M. D., Beckman, R. J., and Conover, W. J., 2000, "A Comparison of Three Methods for Selecting Values of Input Variables in the Analysis of Output From a Computer Code," Technometrics, **42**(1), pp. 55–61.

Downloaded from http://asmedigitalcollection.asme.org/fluidsengineering/article-pdf/144/7/071206/6849053/fe_144_07_071206.pdf by The Pennsylvania State University user on 21 October 2022